Isogeometric semi-Lagrangian analysis for transport problems

Ilham Asmouh[a], Mofdi El-Amrani[b,*], Mohammed Seaid[c]

[a] *International Water Research Institute, University Mohammed VI Polytechnic, Benguerir, Morocco*
[b] *Dpto. Matemáticas Applicada, Ciencia e Ingeniería de Materiales y Tecnología Electrónica, Universidad Rey Juan Carlos, 28933 Móstoles-Madrid, Spain*
[c] *Department of Engineering, University of Durham, South Road, DH1 3LE, UK*

Abstract

Isogeometric analysis (IGA) is combined with the semi-Lagrangian scheme to develop a stable and highly accurate method for the numerical solution of transport problems. An L^2 projection using the non-uniform rational B-splines (NURBS) is proposed for the approximation of the solution at the departure points. The proposed method maintains the advantages of the semi-Lagrangian scheme in reducing the truncation errors and allowing for large CFL numbers in the simulations while the IGA guarantees the exact representation of the geometry of the computational domain. The performance of the isogeometric semi-Lagrangian analysis is demonstrated for a deformational flow problem and the benchmark of a single vortex flow.

Keywords: Isogeometric analysis; Semi-Lagrangian method; L^2 projection; Transport problems.

1. Introduction

Given a two-dimensional bounded domain $\Omega \subset \mathbb{R}^2$ with Lipschitz boundary and a given time interval $[0, T]$, this note proposes a novel isogeometric semi-Lagrangian analysis for the transport equation

$$\frac{\partial u}{\partial t} + \boldsymbol{v}(t, \boldsymbol{x}) \cdot \nabla u = 0, \qquad (t, \boldsymbol{x}) \in (0, T] \times \Omega, \tag{1}$$

where $u(t, \mathbf{x})$ is the concentration of some species and $\boldsymbol{v}\,(t, \boldsymbol{x})$ is the velocity field. We assume that the equation (1) is equipped with well defined initial and boundary conditions depending on the problem under study. Transport problems are essentially characterized by some complicated features such as deformational flows and shear layers which involve steep gradients in their numerical solutions. The semi-Lagrangian methods have been widely applied and proved their efficiency for this class of problems. This note proposes a new isogeometric semi-Lagrangian analysis for solving the transport equation (1) involving high deformational flows and sharp gradients. The idea consists on rewriting the transport equation in terms of Lagrangian coordinates and use the method of characteristics for its time integration. The departure points are approximated using the fourth-order Runge-Kutta scheme while the NURBS functions are used for evaluating the solutions at the departure points. It should be stressed that, in the isogeometric analysis, the control points do not lie on the physical geometry therefore, the NURBS functions are not interpolatory [2]. In the current study, to overcome this drawback in the NURBS functions we consider the L^2 projection introduced in [5]. It should be noted that the L^2-projection for the Galerkin-characteristic solution of incompressible flows proposed in [5] uses the conventional Lagrange basis functions which are only second-order accurate. In the present work, we propose an isogeometric analysis for the semi-Lagrangian solution of transport problems using high-order NURBS functions. This results in an approach with higher accuracy than the one studied in [5]. In addition, as in the conventional finite element methods, the method in [5] uses an approximate geometry whereas the geometry is exactly represented in the case of isogeometric analysis studied here.

*Corresponding author
Email addresses: ilham.asmouh@um6p.ma (Ilham Asmouh), mofdi.elamrani@urjc.es (Mofdi El-Amrani), m.seaid@durham.ac.uk (Mohammed Seaid)

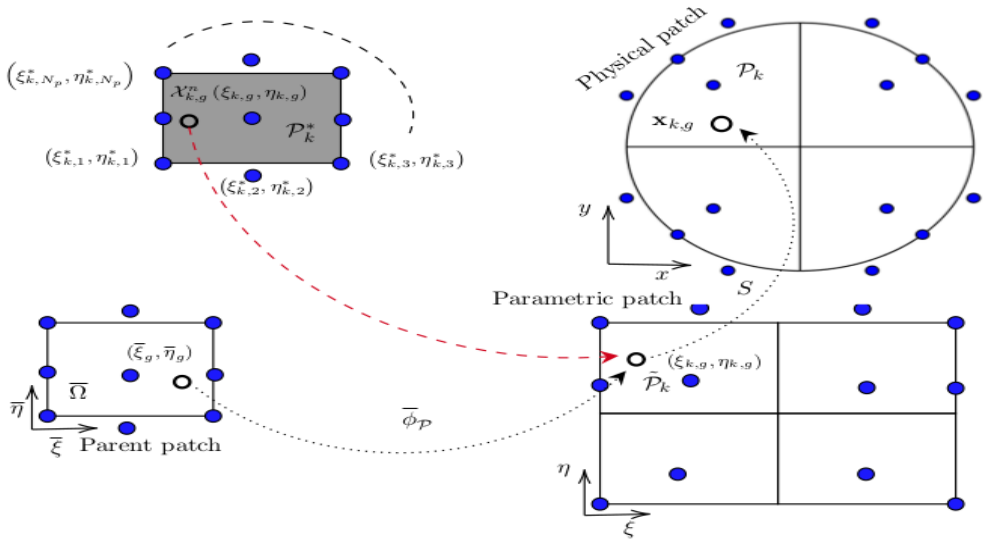

Figure 1: Illustration of the main quantities required for the computation of the departure points.

2. Isogeometric semi-Lagrangian analysis

Given a knot vector Ξ defined as an ordered set of increasing parameters $\Xi = \left\{\xi_1, \xi_2, \ldots, \xi_{m_b+p+1}\right\}$, where m_b denotes the number of basis functions and p is the polynomial order, the NURBS functions are defined by

$$R_i^p(\xi) = \frac{N_i^p(\xi)\omega_i}{\sum_{i=1}^{m_b} N_i^p(\xi)\omega_i}, \tag{2}$$

where $\left\{N_i^p\right\}_{i=1}^{m_b}$ is the set of B-spline basis functions of order p, defined recursively by the Cox-de-Boor recursive formula [10, 4], and $\{\omega_i\}_{i=1}^{m_b}$ is the set of NURBS weights. In two space dimensions, the NURBS surfaces are straightforwardly constructed by considering the tensor product of two NURBS functions $R_i^p(\xi)$ and $R_i^q(\eta)$ as

$$\mathcal{S}^{p,q}(\xi,\eta) = \sum_{i=1}^{m_b}\sum_{j=1}^{l_b} R_i^p(\xi)R_j^q(\eta)B_{i,j}, \tag{3}$$

where $B_{i,j}$ is the vector of control points with m_b and l_b denote the total numbers of control points in x-direction and y-direction, respectively. Note that (3) can also be rewritten in a compact form as

$$\mathcal{S}^{p,q}(\xi,\eta) = \sum_{m=1}^{\text{nDoF}} R_m^{p,q}(\xi,\eta)B_m, \tag{4}$$

where $R_m^{p,q}$ is the basis function defined as $R_m^{p,q}(\xi,\eta) = R_i^p(\xi)R_j^q(\eta)$ and $\text{nDoF} = m_b \times l_b$ is the total number of control points. Here, the computational domain Ω is discretized into of a set of patches $\mathcal{P}_k$ as $\Omega = \cup_{k=1}^{N_p}\Omega_{\mathcal{P}_k}$, with N_p is the total number of patches. The time interval is also divided into sub-intervals $[t_n, t_{n+1}]$ with a length Δt.

2.1. Semi-Lagrangian method

The semi-Lagrangian method is a time stepping scheme for which the time derivative and the convection terms are combined as a directional derivative along the characteristic curves. The Lagrangian treatment in this method greatly reduces the time truncation errors compared to the Eulerian methods and it offers the possibility of using time steps that

exceed those permitted by the CFL stability conditions in the Eulerian-based IGA for the transport problems. As the NURBS functions are not interpolatory [2], we consider in this note the L^2-projection [5] to overcome this drawback. Hence, for each patch $\mathcal{P}_k$ we consider its associated Gauss-Jacobi quadrature points $\boldsymbol{x}_{k,g}$ with the corresponding weights $\omega_{k,g}$ for $g = 1, \ldots, N_{k,g}$ and $N_{k,g}$ is the total number of quadrature points in the patch $\mathcal{P}_k$ [3]. Thus, the characteristic curves $\boldsymbol{\mathcal{X}}(\tau, \boldsymbol{x}_{k,g})$ associated with the transport problem (1) are calculated for each quadrature point $\boldsymbol{x}_{k,g}$ by solving the backward differential equations

$$\begin{aligned} \frac{d\boldsymbol{\mathcal{X}}(\tau, \boldsymbol{x}_{k,g})}{d\tau} &= \boldsymbol{v}(\boldsymbol{\mathcal{X}}(\tau, \boldsymbol{x}_{k,g})), \qquad \forall\ \tau \in [t_n, t_{n+1}], \\ \boldsymbol{\mathcal{X}}(t_{n+1}, \boldsymbol{x}_{k,g}) &= \boldsymbol{x}_{k,g}, \end{aligned} \tag{5}$$

where $\boldsymbol{\mathcal{X}}(\tau, \boldsymbol{x}_{k,g})$ is the departure point defined at time τ of a particle that will arrive in the mesh point $\boldsymbol{x}_{k,g}$ at time t_{n+1}. Note that the semi-Lagrangian methods do not follow the flow particles forward in time, as the Lagrangian schemes do, instead they trace backwards the position at time t_n of particles that will reach the points of a fixed mesh at time t_{n+1}, see Figure 1 for an illustration. To solve the initial-valued problem (5) we use the well-established fourth-order explicit Runge-Kutta method. In general, the departure points $\boldsymbol{\mathcal{X}}(t_n, \boldsymbol{x}_{k,g})$ do not coincide with the spatial position of the point $\boldsymbol{x}_{k,g}$ and thus, the host element where such point belongs should be located using a search-locate procedure, see for instance [5]. Next, integrating the transport equation (1) along the characteristic curves yields

$$u^{n+1}(\boldsymbol{x}) = u^n \circ \boldsymbol{\mathcal{X}}^n(\boldsymbol{x}), \tag{6}$$

where $\boldsymbol{\mathcal{X}}^n(\boldsymbol{x}) = \boldsymbol{\mathcal{X}}(t_n, \boldsymbol{x})$ is a notation to emphasis the dependence of the departure points $\boldsymbol{\mathcal{X}}$ on the mesh point $\boldsymbol{x}$.

2.2. L^2-projection procedure

In the present note, the solution (6) is obtained by a weak formulation using the L^2 projection. Thus, multiplying both sides of (6) by the NURBS functions $R_m^{p,q}$ and integrating over Ω leads to the following weak form

$$\int_\Omega u^{n+1}(\boldsymbol{x}) R_m^{p,q}(\boldsymbol{x})\, d\Omega = \int_\Omega u^n(\boldsymbol{\mathcal{X}}^n) R_m^{p,q}(\boldsymbol{x})\, d\Omega, \qquad m = 1, \ldots, \text{nDoF}. \tag{7}$$

The isogeometric finite element solution $u^{n+1}(\boldsymbol{x})$ is expressed in the following form

$$u^{n+1}(\boldsymbol{x}) = \sum_{l=1}^{\text{nDoF}} U_l^{n+1} R_l^{p,q}(\boldsymbol{x}), \tag{8}$$

where U_l^{n+1} are the unknown nodal coefficients of the solution. Replacing (8) in the left-hand side of (7) we obtain

$$\int_\Omega u^{n+1}(\boldsymbol{x}) R_m^{p,q}(\boldsymbol{x})\, d\Omega = \int_\Omega \sum_{l=1}^{\text{nDoF}} U_l^{n+1} R_l^{p,q}(\boldsymbol{x}) R_m^{p,q}(\boldsymbol{x})\, d\Omega = \sum_{l=1}^{\text{nDoF}} U_l^{n+1} \int_\Omega R_l^{p,q}(\boldsymbol{x}) R_m^{p,q}(\boldsymbol{x})\, d\Omega, \tag{9}$$

Notice that the crucial idea behind the L^2 projection is the computation of the right-hand integral in (7). In the present work, this integral is evaluated using the NURBS functions as

$$\begin{aligned} \int_\Omega u^n(\boldsymbol{\mathcal{X}}^n) R_m^{p,q}(\boldsymbol{x})\, d\Omega &= \sum_{k=1}^{N_e} \int_{\Omega_{\mathcal{P}_k}} u^n \circ \boldsymbol{\mathcal{X}}^n(\boldsymbol{x}) R_m^{p,q}(\boldsymbol{x})\, d\Omega = \sum_{k=1}^{N_e} \int_{\bar\Omega} u^n \circ \boldsymbol{\mathcal{X}}^n(\bar\xi, \bar\eta) R_m^{p,q}(\bar\xi, \bar\eta) \left|J(\bar\xi, \bar\eta)\right|\, d\bar\Omega \\ &\approx \sum_{k=1}^{N_e} \sum_{g=1}^{N_{k,g}} w_{k,g} u^n \circ \boldsymbol{\mathcal{X}}^n(\bar\xi_g, \bar\eta_g) R_m^{p,q}(\bar\xi_g, \bar\eta_g) \left|J(\bar\xi_g, \bar\eta_g)\right| = \sum_{k=1}^{N_e} \sum_{g=1}^{N_{k,g}} w_{k,g} \widetilde{u}_{k,g}^n R_m^{p,q}(\bar\xi_g, \bar\eta_g) \left|J(\bar\xi_g, \bar\eta_g)\right|, \end{aligned} \tag{10}$$

where $\widetilde{u}_{k,g}^n = u^n(\boldsymbol{\mathcal{X}}^n(\boldsymbol{x}_{k,g}))$ denotes the solution calculated at the departure point $\boldsymbol{\mathcal{X}}^n(\boldsymbol{x}_{k,g})$, $w_{k,g}$ are the weights generated from the Gauss-Jacobi quadrature rule and $\left|J(\bar\xi_g, \bar\eta_g)\right|$ denotes the determinant of the composition of the Jacobian from

the parent space $\bar{\Omega}$ to the parametric space $\tilde{\Omega}$ and the Jacobian from parametric space $\tilde{\Omega}$ to the physical space Ω [10]. Here, the values $\widetilde{u}^n_{k,g}$ are computed as

$$\widetilde{u}^n_{k,g} := u^n(\boldsymbol{\mathcal{X}}^n(\boldsymbol{x}_{k,g})) = \sum_{d=1}^{N_p} u^n(\xi^*_{k,d}, \eta^*_{k,d}) R^{p,q}_d(\boldsymbol{\mathcal{X}}^n(\boldsymbol{x}_{k,g})), \tag{11}$$

where $u^n(\xi^*_{k,d}, \eta^*_{k,d})$ are the known solutions at the control points $(\xi^*_{k,d}, \eta^*_{k,d})$ of the host patch $\mathcal{P}^*_k$ where the departure point $\boldsymbol{\mathcal{X}}^n(\boldsymbol{x}_{k,g})$ belongs. Here, N_p is the total number of control points within the host patch $\mathcal{P}^*_k$ which is directly related to the order of NURBS basis functions, see Figure 1 for an illustration. Thus, inserting the approximations (9) and (10) in (7) yields

$$\sum_{l=1}^{\text{nDoF}} a_{ml} U^{n+1}_l = b^n_m, \qquad m = 1, \ldots, \text{nDoF}, \tag{12}$$

where

$$b^n_m = \sum_{k=1}^{N_e} \sum_{g=1}^{N_{k,g}} w_{k,g} \widetilde{u}^n_{k,g} R^{p,q}_m(\bar{\xi}_g, \bar{\eta}_g) \left| J(\bar{\xi}_g, \bar{\eta}_g) \right|, \tag{13}$$

and

$$\begin{aligned} a_{ml} &= \int_\Omega R^{p,q}_l(\boldsymbol{x}) R^{p,q}_m(\boldsymbol{x})\, d\Omega = \sum_{k=1}^{N_e} \int_{\Omega_{\mathcal{P}_k}} R^{p,q}_l(\boldsymbol{x}) R^{p,q}_m(\boldsymbol{x})\, d\Omega_{\mathcal{P}_k}, \\ &= \sum_{k=1}^{N_e} \int_{\bar{\Omega}} R^{p,q}_l(\bar{\xi}, \bar{\eta}) R^{p,q}_m(\bar{\xi}, \bar{\eta}) \left| J(\bar{\xi}, \bar{\eta}) \right| \, d\bar{\Omega} \approx \sum_{k=1}^{N_e} \sum_{g=1}^{N_{k,g}} w_{k,g} R^{p,q}_l(\bar{\xi}_g, \bar{\eta}_g) R^{p,q}_m(\bar{\xi}_g, \bar{\eta}_g) \left| J(\bar{\xi}_g, \bar{\eta}_g) \right|. \end{aligned} \tag{14}$$

Note that the equation (12) can also be assembled in a global matrix-vector form as

$$[\mathbf{A}] \left\{ \mathbf{u}^{n+1} \right\} = \{ \mathbf{b}^n \}, \tag{15}$$

where $[\mathbf{A}]$ is the nDoF $\times$ nDoF-valued isogeometric L^2-projection matrix with entries a_{ml}, $\left\{ \mathbf{u}^{n+1} \right\}$ is the nDoF-valued vector of unknown values of the solution U^{n+1}_m at time t_{n+1}, and $\{\mathbf{b}^n\}$ is the nDoF-valued vector of the known right-hand side with entries b^n_m. In our simulations, the linear system of algebraic equations (15) is solved using the multifrontal direct solver proposed in [1].

3. Numerical results

Two well-established examples of transport problems are considered in this section to demonstrate the performance of the proposed isogeometric semi-Lagrangian analysis. In our results reported herein, the CFL number is fixed to CFL = 5 and the time stepsize Δt is adjusted at each time step according to the relation [9]

$$\text{CFL} = \|\boldsymbol{v}\|_\infty \frac{\Delta t}{h} (2p + 1), \tag{16}$$

where h is space steptize. Note that to reduce the computational cost, the time steps Δt are chosen as large as possible in our simulations. This would make most explicit Eulerian-based IGA methods noncompetitive, since they are subject to stability restriction conditions for the convection terms. It should be noted that the knot points are located in the parametric domain whereas the numerical results are visualized in the physical domain. Hence, a NURBS-based mesh is the image of knot lines in the physical space and to construct a geometric object, we multiply the NURBS functions by the physical coordinates. Notice also that the k-refinement strategy is adopted in all our numerical examples. Here, two initial open and uniform knot vectors along the x and y directions are elevated to the desired order and then followed by an h-refinement technique as discussed in [8]. This means that for a given set of initial knot vectors $\Xi^a = \{0, 0, 1, 1\}$ and $\Xi^b = \{0, 0, 1, 1\}$ of orders $p = q = 1$, we firstly elevate the orders p and q to $p + 1$ and $q + 1$

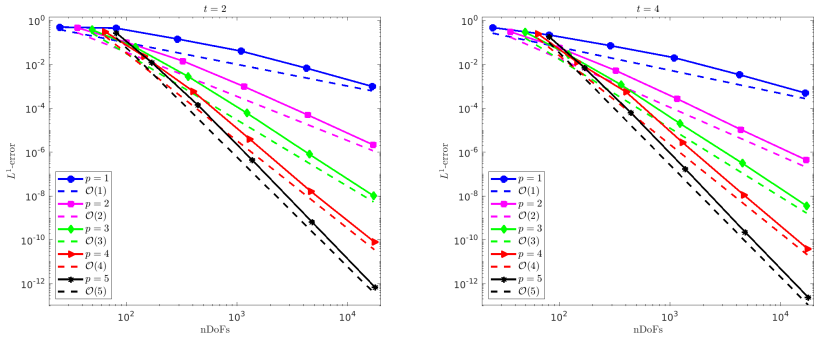

Figure 2: Convergence plots in the L^1-error for the deformational flow problem on a mesh with 32×32 patches at two different instants.

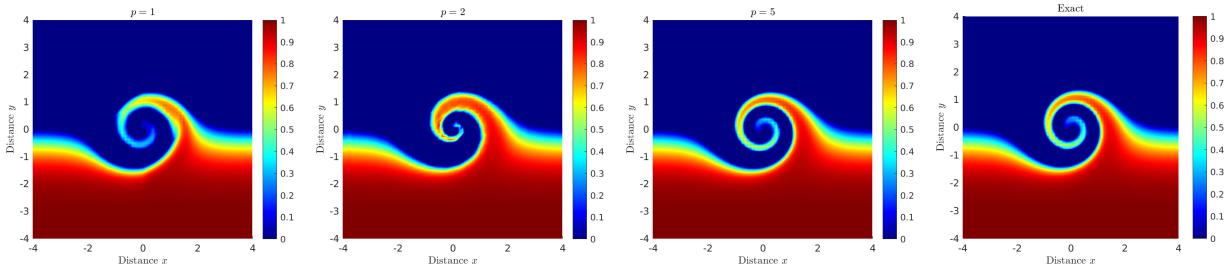

Figure 3: Snapshots of the solutions obtained for the deformational flow problem at time $t = 4$ using different NURBS orders.

respectively to obtain the knot vectors $\Xi^{a'} = \{0, 0, 0, 1, 1, 1\}$ and $\Xi^{b'} = \{0, 0, 0, 1, 1, 1\}$ then, we insert new knots in the x and y directions. By doing so, full continuity (*i.e.*, the C^p in x direction and the C^q in y direction) are maintained across the elements. The same process is continued up to the desired order which is restricted in the current note to $p = q = 5$.

3.1. Deformational flow problem

Our first example consists of the deformational flow widely served as a prototype to examine the performance of transport methods [7]. The problem (1) is solved in the spatial domain $\Omega = [-4, 4] \times [-4, 4]$ equipped with a highly deformational flow field defined by a steady circular vortex with tangential velocity

$$v_t(x, y) = v_0 \text{sech}^2(r) \tanh(r), \qquad r = \sqrt{x^2 + y^2},$$

where $v_0 = 2.58$ is a constant selected to ensure that the maximum value of v_t is less than unity. Initial and boundary conditions are obtained from the analytical solution

$$u(t, x, y) = -\tanh\left(\frac{y}{\delta}\cos\left(\frac{v_t}{r}t\right) - \frac{x}{\delta}\sin\left(\frac{v_t}{r}t\right)\right), \tag{17}$$

with $\delta = 0.05$ is a parameter controlling the steepness of the solution (17). In all our simulations, a uniform mesh consisting of 32×32 grids of squared patches with side length $h = 1/32$ is considered. Refinements are performed by the k-refinement method, and the numerical solutions are computed using different NURBS degrees ranging from $p = 1$ to $p = 5$. In Figure 2 we present the convergence plots of L^1-error against the number of degrees of freedom using $p = 1$, 2, 3, 4 and 5 at two instants $t = 2$ and $t = 4$. It is clear that the slopes of the convergence plots are consistent with the convergence rates of the considered NURBS degrees for this test example. For instance, at $t = 4$, the slopes of the convergence plots for linear, quadratic, cubic, quartic and quintic NURBS are 0.99, 2.01, 3.02, 4.01 and 5.00, respectively. Keeping a NURBS order fixed and performing a series of h-refinement, starting with a mesh

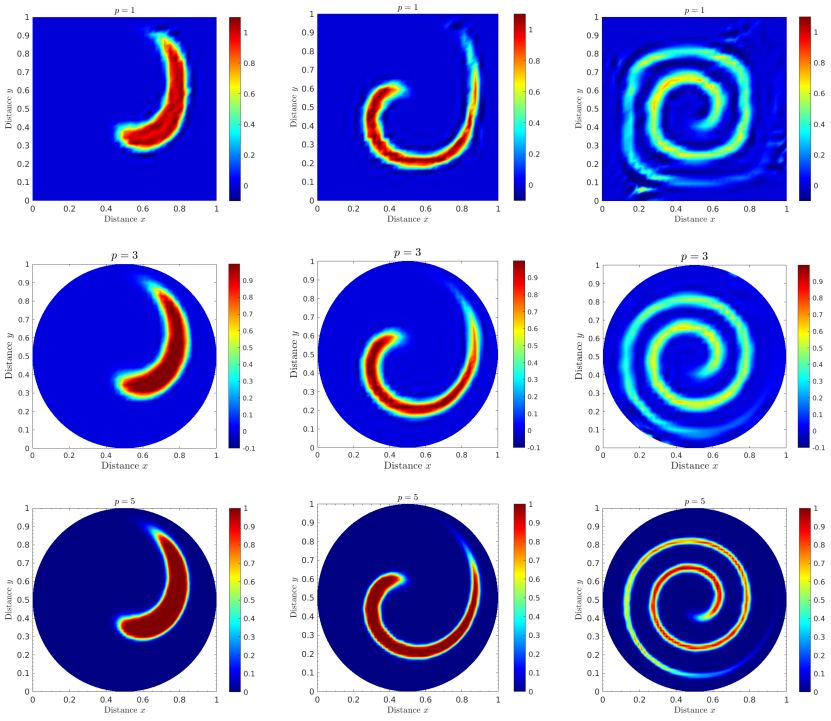

Figure 4: Snapshots of the solutions obtained for the single-vortex flow problem at time $t = 0.5$ (first column), $t = 1$ (second column) and $t = 4$ (third column) using different NURBS orders.

of 4×4 patches, results in a decrease of all errors. Moreover, the L^1-error behaves as $O(p)$ for all considered NURBS orders as illustrated in Figure 2. Regarding the order elevation, we observe from this figure that the p-refinement does not improve the convergence for very coarse meshes. However, it is clear that increasing the NURBS order results in a highly improved accuracy at around only nDoFs $= 10^2$ (which is a very reduced total number of degrees of freedom compared to the nDoFs needed in conventional finite element method to obtain the same behavior). Notice that this fast decrease of errors is essentially related to the k-refinement technique offered by IGA. To further illustrate effects of the k-refinement on the accuracy of the obtained results, which consists essentially on increasing the smoothness over elements and eventually improves the accuracy and the efficiency compared with classical p-refinement, observe that for example using $p = 2$ we obtain an accuracy of L^1-error $= 10^{-4}$ at around nDoFs $= 7 \times 10^3$. However, the same accuracy is attained for $p = 5$ at just around nDoFs $= 8 \times 10^2$, means about $\frac{1}{8}$ times the required nDoFs for $p = 2$. Notice that with k-refinement, $p = 2$ and $p = 5$ attain respectively the C^1 and C^4 continuities. Figure 3 illustrates the snapshots of the computed solutions at time $t = 4$ using $p = 1$, 2 and 5 along with the exact solution. Clearly, the linear solution produces inaccurate results whereas, the quadratic solution still exhibits large numerical dissipation and oscillations at the areas of steep gradients. The solution obtained using the quintic order matches the analytical solution. It should be pointed out that the performance of the proposed method is very attractive since the computed solutions are highly accurate and stable even when coarse meshes and large values of CFL are used in the simulations without requiring stabilization techniques as those used in the Eulerian-based finite element methods for transport and convection-dominant problems.

3.2. Single-vortex flow problem

In this example we illustrate the ability of the proposed method to resolve high gradients at scales of the mesh which occur in stretching and tearing flows by a velocity field involving the single vortex flow described in [6]. Here, we solve (1) in the squared domain $\Omega = [0, 1] \times [0, 1]$ with the initial condition defined by a circular body of radius

0.15 centered at $(0.5, 0.75)^\top$ which is evolved by a single vortex flow field. The velocity field is given by

$$u(t,x,y) = \sin^2(\pi x)\sin(2\pi y)\cos\left(\frac{\pi t}{T}\right), \qquad v(t,x,y) = -\sin(2\pi x)\sin^2(\pi y)\cos\left(\frac{\pi t}{T}\right),$$

where $T = 8$ is the time period at which the flow returns to its initial shape. In Figure 4 we display the snapshots of the computed solutions at times $t = 0.5$, 1 and 4 on a mesh with 32×32 patches using $p = 1$, 3 and 5. Note that a rational quadratic basis is the minimum order capable of representing a circular geometry. Hence, the linear order is executed on a square domain, while the cubic and quintic orders are equipped with a circular domain. It is clear that the linear solution fails to produce accurate results and spurious oscillations are detected as time evolves in both solutions with $p = 1$ and $p = 3$. By elevating the NURBS order to $p = 5$, high accuracy is achieved and the computed results are in good agreement with those reported in [6]. Indeed, one of the interesting features of NURBS is that the geometric object is exactly represented and explicitly defined by the rational polynomials. Thus, the h-refinement keeps exactly the same geometric object which means that if we insert new knots we do not change the geometry. This property is also conserved with p-refinement. Starting all over with the same object, we can p-refine while keeping the continuity the same. For example C^1 quadratic NURBS become C^1 cubic NURBS through order elevation. In this case, the mesh is the same and the knots are moving around to preserve the geometry. The presented results also demonstrate that the proposed isogeometric semi-Lagrangian analysis is suited for the prediction of transport by deformational flows.

4. Conclusions

In this note, a combination of IGA and semi-Lagrangian method is proposed for the numerical solution of transport problems. A Galerkin L^2 projection using the NURBS basis functions is implemented for the approximation of the solution at the departure points. It is proven by numerical results for two test examples that the k-refinement strategy, which is unique to IGA and it does not have analogy in the conventional finite element methods, when combined with the semi-Lagrangian time stepping, results in highly stable and accurate solutions on coarse meshes and using large time steps. The computational costs required in Eulerian-based IGA methods can be strongly reduced using the presented semi-Lagrangian approach. It should also be noted that to overcome the limitations inherent in the tensor-product nature of B-splines and NURBS and also reducing computational costs, a local refinement technique could be beneficial for our isogeometric semi-Lagrangian analysis for transport problems. In this case, using the transport nature of the problem under study, a local refinement would allow that the NURBS mesh is refined in some specific areas and does not propagate through the entire patch. Future works should include three-dimensional transport problems, the incorporation of diffusion operators, and extension to incompressible Navier-Stokes equations using local refinement techniques.

References

[1] P.R. Amestoy, I.S. Duff, J.Y. L'Excellent, and J. Koster. A fully asynchronous multifrontal solver using distributed dynamic scheduling. *SIAM J. Matrix Anal. Appl.*, 23(1):15–41, 2001.

[2] Y. Bazilevs, L.B. da Veiga, J.A. Cottrell, T.J.R. Hughes, and G. Sangalli. Isogeometric analysis: approximation, stability and error estimates for h-refined meshes. *Math. Models Methods Appl. Sci.*, 16(07):1031–1090, 2006.

[3] A. Chernov and C. Schwab. Exponential convergence of Gauss-Jacobi quadratures for singular integrals over simplices in arbitrary dimension. *SIAM J. Numer. Anal.*, 50(3):1433–1455, 2012.

[4] J.A. Cottrell, T.JR. Hughes, and Y. Bazilevs. *Isogeometric analysis: toward integration of CAD and FEA*. John Wiley & Sons, 2009.

[5] M. El-Amrani and M. Seaid. An L^2-projection for the Galerkin-characteristic solution of incompressible flows. *SIAM J. Sci. Comput.*, 33(6):3110–3131, 2011.

[6] D. Enright, F. Losasso, and R. Fedkiw. A fast and accurate semi-lagrangian particle level set method. *Comput. Struct.*, 83(6-7):479–490, 2005.

[7] E.V. Hólm. A fully two-dimensional, non-oscillatory advection scheme for momentum and scalar transport equations. *Mon. Wea. Rev.*, 123:536–552, 1995.

[8] T.J.R. Hughes, J.A. Cottrell, and Y. Bazilevs. Isogeometric analysis: CAD, finite elements, NURBS, exact geometry and mesh refinement. *Computer Methods in Applied Mechanics and Engineering*, 194(39-41):4135–4195, 2005.

[9] J. Kou, A. Hurtado-de Mendoza, S. Joshi, S. Le Clainche, and E. Ferrer. Eigensolution analysis of Immersed boundary method based on volume penalization: Applications to high-order schemes. *J. Comput. Phys.*, page 110817, 2021.

[10] V.P. Nguyen, C. Anitescu, S.PA. Bordas, and T. Rabczuk. Isogeometric analysis: an overview and computer implementation aspects. *Math. Comput. Simul.*, 117:89–116, 2015.